Energy-Based Visualization of 2D Flow Fields

Karsten Hanser, Stefan Meggendorfer, Peter Hügel, Florian Fallenbüchel, Hafiz Muhammad Fahad and Filip Sadlo
IWR, Heidelberg University, Im Neuenheimer Feld 205, Heidelberg, Germany

Keywords: Flow Visualization, Bernoulli's Principle, Energy Conversion.

Abstract: In this paper, we present a novel approach for energy-based flow visualization. Inspired by Bernoulli's principle, which is limited to steady inviscid flow, we derive a set of energies whose sum is conserved along pathlines in 2D time-dependent viscous flow. We present an interactive approach for visual analysis based on these quantities, as well as a compact color-coded representation. This enables effective analysis of energy conversion along selected pathlines, as well as its spatial coherence. We exemplify the utility of our approach using results from computational fluid dynamics and flow in elastic porous media.

1 INTRODUCTION

Many problems in science and engineering require vector field representations. A prominent example are flow problems, which are often addressed by computational fluid dynamics (CFD) by means of numerical solution of the Navier–Stokes (NS) equations.

There exists a wide spectrum of flow visualization techniques for analyzing vector fields from CFD. On the one hand, there are geometric approaches, such as arrow glyphs and streamlines, which show the overall structure of a flow, but fail at revealing underlying physical mechanisms. On the other hand, there are physically based approaches, such as the λ_2 vortex criterion, which often involve derivatives of the vector fields and sometimes additional quantities such as the pressure field. Either way, most flow visualization techniques aim at a simplified representation of flow, often providing a "segmentation" into regions of similar behavior or extraction of respective boundaries.

In this paper, we investigate the analysis of flow fields with regard to their immanent energies. We present an approach that, on the one hand, enables the analysis of energy conversion in flows for a better understanding of the involved physical mechanisms. On the other hand, our approach enables the identification of regions of physically similar behavior with respect to these energies. Our approach is inspired by Bernoulli's principle, which, however, is applicable only to inviscid stationary flow. We extend it to viscous time-dependent flow, and derive from it a technique for interactive visual analysis of flow fields.

The contributions of this paper include:

- a set of energy quantities whose sum is conserved along trajectories, up to solver-induced error,
- an approach to quantify that solver-induced error and relate it to our quantities,
- an interactive exploration approach enabling detailed analysis of energy conversion and the physical mechanisms along trajectories, and
- an approach to reveal the regions of qualitatively similar behavior with respect to energy dynamics.

2 RELATED WORK

The most closely related work in the field of fluid dynamics is Bernoulli's Hydrodynamica (Bernoulli, 1738), which presents the concept later denoted Bernoulli's principle, detailed in Section 3.

Previous work in the context of energy-based flow visualization includes proper orthogonal decomposition for separating different scales with respect to energy (Pobitzer et al., 2011), and a graph based approach, which focuses on the conversion and transportation of internal and kinetic energy (Fernandes et al., 2017). The focus of our work, in contrast, is on decomposition, transport, and conversion of different energy types along pathlines.

Less closely related are physically based criteria, such as λ_2 (Jeong and Hussain, 1995) for vortex extraction, and interaction between shear flow and vorti-

Hanser, K., Meggendorfer, S., Hügel, P., Fallenbüchel, F., Fahad, H. and Sadlo, F.
Energy-Based Visualization of 2D Flow Fields.
DOI: 10.5220/0007359602500258
In *Proceedings of the 14th International Joint Conference on Computer Vision, Imaging and Computer Graphics Theory and Applications (VISIGRAPP 2019)*, pages 250-258
ISBN: 978-989-758-354-4

ces (Schafhitzel et al., 2011; Sadlo et al., 2006). Other approaches employ physical principles for visualizing advection properties, such as schlieren flow visualization (Brownlee et al., 2010) and virtual rheoscopic fluids (Barth and Burns, 2007).

3 BERNOULLI'S PRINCIPLE

Bernoulli presented in his early work on hydrodynamics (Bernoulli, 1738) his principle, which relates kinetic, pressure, and potential energy. Assuming inviscid steady flow, i.e., flow that has zero viscosity and no time dependency, his principle states that energy is conserved along streamlines, e.g., if velocity increases along a streamline, it implies a respective decrease of pressure energy and/or potential energy. In other words, it describes the transformation of energy along streamlines in fluid flow.

A *streamline*

$$\boldsymbol{\xi}^t_{\mathbf{x}_0}(s) := \mathbf{x}_0 + \int_0^s \mathbf{u}\left(\boldsymbol{\xi}^t_{\mathbf{x}_0}(\sigma), t\right) d\sigma \qquad (1)$$

is obtained by solving an initial value problem (IVP) in a single time step t of the (potentially unsteady) n-dimensional vector field $\mathbf{u}(\mathbf{x},t)$ defined on a domain $\Omega \subseteq \mathbb{R}^n$, with $\mathbf{x} \in \Omega$ and $\mathbf{u} \in \mathbb{R}^n$. That is, one starts the integration at a seed point $\mathbf{x}_0 \in \Omega$ with $\boldsymbol{\xi}^t_{\mathbf{x}_0}(0) = \mathbf{x}_0$, and integrates a curve tangential to the vector field $\mathbf{u}(\mathbf{x},t)$ for a given duration s, keeping physical time t fixed. On the other hand, a *pathline*

$$\boldsymbol{\xi}_{\mathbf{x}_0,t_0}(t) := \mathbf{x}_0 + \int_{t_0}^t \mathbf{u}\left(\boldsymbol{\xi}_{\mathbf{x}_0,t_0}(\tau), \tau\right) d\tau \qquad (2)$$

is obtained by solving an IVP "including" physical time, i.e., by starting integration at a seed point $\mathbf{x}_0$ and seed time t_0, and integrating along the time-dependent vector field $\mathbf{u}(\mathbf{x},t)$, that is, the integration parameter is physical time t. Notice, that in steady vector fields, streamlines and pathlines are identical.

According to Bernoulli's principle, along such a streamline in steady inviscid flow, i.e., at each point $\mathbf{x} = \boldsymbol{\xi}^t_{\mathbf{x}_0}(s)$, the sum of kinetic energy

$$E_u(\mathbf{x},t) := \frac{\|\mathbf{u}(\mathbf{x},t)\|^2}{2}, \qquad (3)$$

pressure energy

$$E_p(\mathbf{x},t) := \frac{p(\mathbf{x},t)}{\rho}, \qquad (4)$$

and potential energy

$$E_h(\mathbf{x}) := gh(\mathbf{x}), \qquad (5)$$

stays constant, i.e., $E_u(\mathbf{x},t) + E_p(\mathbf{x},t) + E_h(\mathbf{x}) = \text{const.}$, with pressure $p(\mathbf{x},t)$, density of the fluid ρ, $h(\mathbf{x})$ the height of point $\mathbf{x}$, and gravity g.

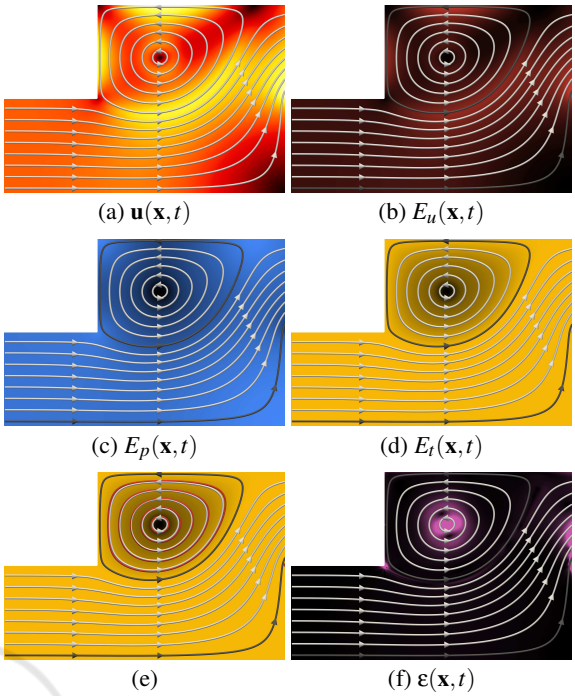

(a) $\mathbf{u}(\mathbf{x},t)$ (b) $E_u(\mathbf{x},t)$ (c) $E_p(\mathbf{x},t)$ (d) $E_t(\mathbf{x},t)$ (e) (f) $\varepsilon(\mathbf{x},t)$

Figure 1: Inviscid steady flow past a back-facing step. (a) Velocity magnitude (low-black; high-yellow), with streamlines (white). (b) Kinetic energy $E_u(\mathbf{x},t)$ (low-black; high-red) is not constant along streamlines, and neither is pressure energy $E_p(\mathbf{x},t)$ (c) (low-black; high-blue). (d) Total energy $E_t(\mathbf{x},t) = E_u(\mathbf{x},t) + E_p(\mathbf{x},t)$, however, is constant up to small deviations. Isolines (red) of $E_t(\mathbf{x},t)$ and streamlines (white and gray) (e) deviate slightly due to inaccuracies of the simulation and derivative estimation, which we quantify as solver error $\varepsilon(\mathbf{x},t)$ (f) (0-black; 0.1-magenta).

Figure 1 illustrates the principle, at the example of a simple inviscid ($\nu = 0$) steady 2D flow simulation obtained with the Gerris flow solver (Popinet, 2007). In this example (and the following), gravity has been set to zero for simulation, resulting in zero potential energy everywhere, i.e., there is only conversion between kinetic and pressure energy here. Notice, that the focus of this paper is flow visualization, i.e., the input to our technique is the simulated fields $\mathbf{u}(\mathbf{x},t)$, $p(\mathbf{x},t)$, as well es density ρ and viscosity ν.

It is apparent that $E_u(\mathbf{x},t)$ (Figure 1(b)) is not uniform along the streamlines, and that neither is $E_p(\mathbf{x},t)$ (Figure 1(c)). Nevertheless, their sum, which we denote total energy $E_t(\mathbf{x},t) := E_u(\mathbf{x},t) + E_p(\mathbf{x},t)$, is almost constant (Figure 1(d)), as can be seen when comparing the streamlines to isolines of $E_t(\mathbf{x},t)$ (Figure 1(e)). The small deviations between streamlines and isolines of E_t stem from inaccuracies of the simulation and derivative estimation during visualization.

To assess such inaccuracies, we derive a quantity which we denote *solver error* $\varepsilon(\mathbf{x},t)$ (Figure 1(f)).

The numerical solver aims at solving the NS equation

$$\frac{D\mathbf{u}(\mathbf{x},t)}{Dt} = -\frac{\nabla p(\mathbf{x},t)}{\rho} + \nu\Delta\mathbf{u}(\mathbf{x},t), \quad (6)$$

with material derivative

$$\frac{D\mathbf{u}(\mathbf{x},t)}{Dt} := \frac{\partial\mathbf{u}(\mathbf{x},t)}{\partial t} + (\nabla\mathbf{u}(\mathbf{x},t))\,\mathbf{u}(\mathbf{x},t), \quad (7)$$

density ρ, Laplacian Δ, and kinematic viscosity ν. However, due to inaccuracies (nonzero solver residuals, as well as potential inconsistencies between derivative estimation in the solver and estimation during our visualization process), the left hand side is in general not identical to the right hand side when the terms of Equation 6 are computed from the simulated fields $\mathbf{u}(\mathbf{x},t)$ and $p(\mathbf{x},t)$. This motivates us to obtain ε as the discrepancy between the two sides, i.e.,

$$\varepsilon(\mathbf{x},t) := \frac{1}{\mu}\left\|\frac{D\mathbf{u}(\mathbf{x},t)}{Dt} + \frac{\nabla p(\mathbf{x},t)}{\rho} - \nu\Delta\mathbf{u}(\mathbf{x},t)\right\|, \quad (8)$$

normalized by μ, which is the average of the magnitude of $D\mathbf{u}(\mathbf{x},t)/Dt$ over the domain Ω:

$$\mu := \frac{1}{\mathrm{vol}(\Omega)}\int_\Omega \left\|\frac{D\mathbf{u}(\mathbf{x},t)}{Dt}\right\| d\Omega, \quad (9)$$

with $\mathrm{vol}(\Omega)$ being the volume (area) of the domain.

4 METHOD

The majority of fluid dynamics problems involves time dependency and necessitates nonzero viscosity, which strongly limits the applicability of Bernoulli's principle. Our main aim in this work, is to address both of these issues, i.e., to derive a concept that enables energy-based flow visualization in time-dependent viscous flow. Whereas we formulate our approach here for 2D flows, its extension to 3D domains would be straightforward in large parts.

4.1 Derivation of Energies

Let us start with a steady CFD simulation of a flow around an obstacle. Again, gravity g was set to zero for simulation, but in this case, the modeled fluid has nonzero kinematic viscosity ν, leading to a wake behind the obstacle exhibiting low velocities (Figure 2(a)). The kinetic energy field $E_u(\mathbf{x},t)$ (Figure 2(c)) and the pressure energy $E_p(\mathbf{x},t)$ (Figure 2(e)) can be easily computed according to Equations 3 and 4 using the simulated fields $\mathbf{u}(\mathbf{x},t)$ and $p(\mathbf{x},t)$. However, if these energies are summed up to obtain the total energy $E_t(\mathbf{x},t)$, the resulting field (Figure 2(g)) is not constant along streamlines, in contrast to the inviscid case from Section 3 (Figure 1(d)). The reason for this discrepancy is the nonzero viscosity, which is violating the assumptions of Bernoulli's principle. That is, velocity undergoes diffusion due to the viscosity (according to the rightmost term $\nu\Delta\mathbf{u}(\mathbf{x},t)$ in Equation 6). In other words, the internal friction in the flow "tries to minimize" the gradient of the velocity field and thus causes kinetic energy to "diffuse". The direction of this diffusion is not constrained to directions along streamlines, and therefore E_t is, in general, not constant along a streamline in viscous flow.

An interesting observation is, however, that since the Navier–Stokes equation (Equation 6) represents the material derivative of velocity $\mathbf{u}(\mathbf{x},t)$, it describes the acceleration of a fluid parcel at location $\mathbf{x}$ and time t. On the other hand, Bernoulli's principle involves the variation of kinetic energy E_u along a streamline. The difference of kinetic energy between two points s_0 and s_1 on such a streamline has to equal the total work between these points, and since work equals the integral of force along a path, we obtain

$$E_u(\mathbf{x}_1,t) = E_u(\mathbf{x}_0,t) + \int_{s_0}^{s_1} \frac{D\mathbf{u}(\boldsymbol{\xi}^t_{\mathbf{x}_0}(s),t)}{Dt}\cdot d\mathbf{s}, \quad (10)$$

with $\mathbf{x}_0 = \boldsymbol{\xi}^t_{\mathbf{x}_0}(s_0)$ and $\mathbf{x}_1 = \boldsymbol{\xi}^t_{\mathbf{x}_0}(s_1)$ being the respective positions on the streamline, and line element $d\mathbf{s} := \mathbf{u}(\boldsymbol{\xi}^t_{\mathbf{x}_0}(s),t)ds$. Notice that E_u is a specific energy in Bernoulli's formulation, and therefore we do not need to multiply the material derivative with density ρ to obtain $E_u(\mathbf{x}_1,t)$. Notice also that since pathlines and streamlines are identical in steady flow, and since the Navier–Stokes equation also holds for unsteady flow, we can replace in Equation 10 the streamline $\boldsymbol{\xi}^t_{\mathbf{x}_0}$ by a pathline $\boldsymbol{\xi}_{\mathbf{x}_0,t_0}$ in this example (and in general, as we will see later).

Altogether, Equation 10 provides an alternative approach for computing $E_u(\mathbf{x},t)$, i.e., at time t, we can start a pathline at point $\mathbf{x}$, integrate it backward in time (in reverse flow direction) until time t_α (with $t_\alpha < t$), and evaluate the line integral accordingly:

$$\tilde{E}_u(\mathbf{x},t) = C_u + \int_t^{t_\alpha} \frac{D\mathbf{u}(\boldsymbol{\xi}_{\mathbf{x},t}(\tau),\tau)}{Dt}\cdot d\boldsymbol{\tau}, \quad (11)$$

with line element $d\boldsymbol{\tau} := \mathbf{u}(\boldsymbol{\xi}_{\mathbf{x},t}(\tau),\tau)d\tau$, and pathline

$$\boldsymbol{\xi}_{\mathbf{x},t}(\tau) := \mathbf{x} + \int_t^\tau \mathbf{u}\left(\boldsymbol{\xi}_{\mathbf{x},t}(\tau),\tau\right) d\tau \quad (12)$$

with $\tau < t$. C_u is an integration constant, which needs to be chosen. Notice that we denote our result *integrated kinetic energy* $\tilde{E}_u$, in contrast to Bernoulli's kinetic energy E_u.

Figure 2(d) shows $\tilde{E}_u(\mathbf{x},t)$ for $C_u = 0$, with reverse integration duration of 100 seconds. For this integration duration, the pathlines either reach the inlet at the left boundary, or stay in the recirculation

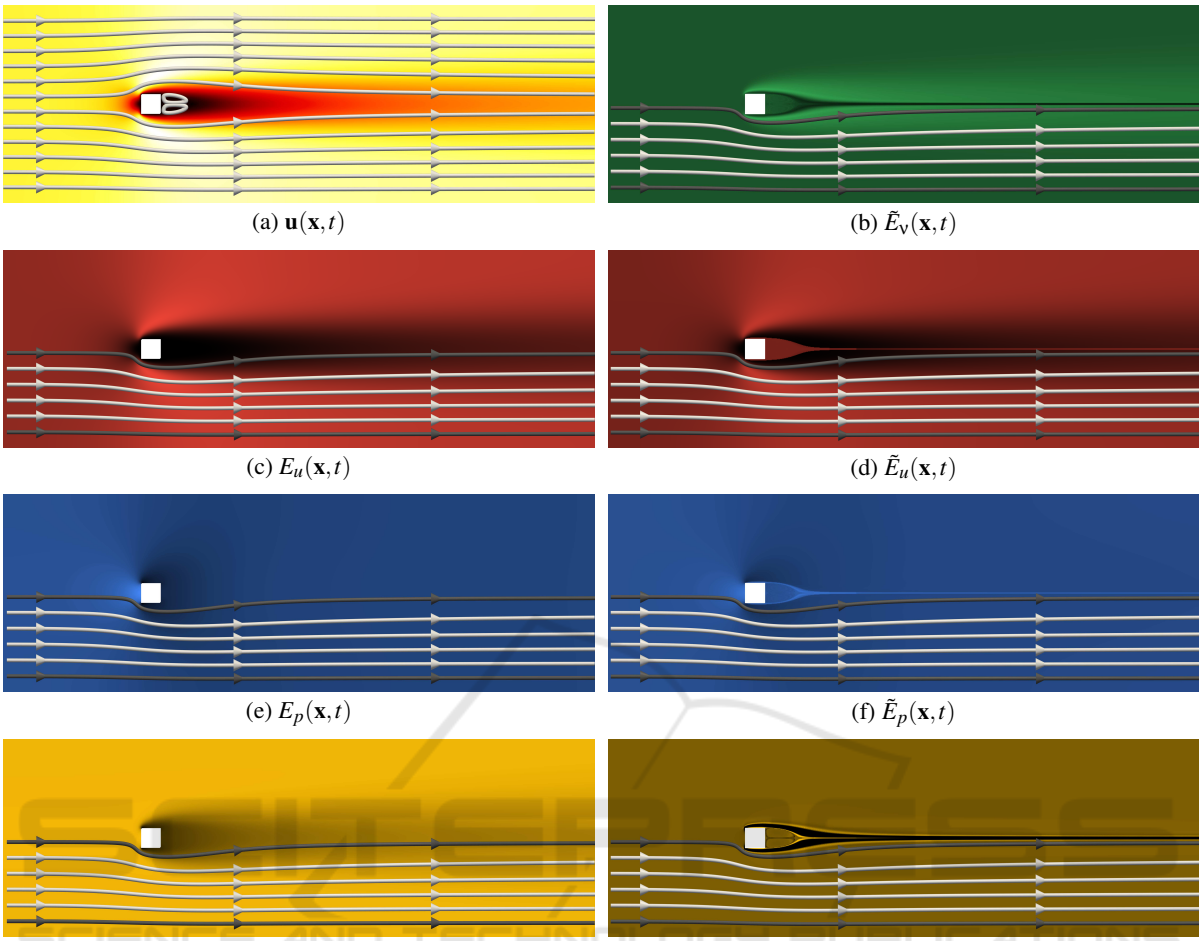

(a) $\mathbf{u}(\mathbf{x},t)$ (b) $\tilde{E}_\nu(\mathbf{x},t)$

(c) $E_u(\mathbf{x},t)$ (d) $\tilde{E}_u(\mathbf{x},t)$

(e) $E_p(\mathbf{x},t)$ (f) $\tilde{E}_p(\mathbf{x},t)$

(g) $E_t(\mathbf{x},t)$ (h) $\tilde{E}_t(\mathbf{x},t)$

Figure 2: Steady viscous flow around obstacle, from left to right. (a) Velocity $\mathbf{u}(\mathbf{x})$ together with streamlines (white). (b) Integrated diffusion energy $\tilde{E}_\nu(\mathbf{x})$, according to Equation 15, with two selected streamlines (gray). (c) Kinetic energy $E_u(\mathbf{x})$, computed locally according to Equation 3. (d) Integrated kinetic energy $\tilde{E}_u(\mathbf{x})$ (Equation 11). (e) Pressure energy $E_p(\mathbf{x})$ and (f) integrated pressure energy $\tilde{E}_p(\mathbf{x},t)$ (Equation 14). (g) Total energy $E_t(\mathbf{x})$ is not conserved along streamlines, whereas integrated total energy $\tilde{E}_t$ is, i.e., $\tilde{E}_u+\tilde{E}_p+\tilde{E}_\nu=$ const. is our counterpart to Bernoulli's principle for unsteady viscous flow.

region right to the obstacle. Since the inlet velocity is constant along the inlet, Figure 2(d) is, up to an additive constant, identical to Figure 2(c), except for the region behind the obstacle. The reason why $\tilde{E}_u(\mathbf{x},t)$ in that region has values different from $E_u(\mathbf{x},t)$, is that setting $C_u=0$ there is not consistent with setting $C_u=0$ at the inlet. While one could set $C_u=E_u(\boldsymbol{\xi}^-_{\mathbf{x},t}(t_\alpha))$, i.e., to the value of E_u at the "upstream end" of the pathline, such an evaluation cannot be achieved for our integrated diffusion energy introduced below. Therefore, we set $C_u=0$.

If we bring the right hand side of Equation 6 to the left side, we have three terms on the left hand side that sum up to zero, i.e.,

$$\frac{D\mathbf{u}(\mathbf{x},t)}{Dt}+\frac{\nabla p(\mathbf{x},t)}{\rho}-\nu\Delta\mathbf{u}(\mathbf{x},t)=0, \qquad (13)$$

or, in other words, three terms whose sum is constant along a pathline.

The same procedure as for $\tilde{E}_u(\mathbf{x},t)$ can be carried out with respect to the pressure term, leading to the *integrated pressure energy*

$$\tilde{E}_p(\mathbf{x},t)=C_p+\int_t^{t_\alpha}\frac{\nabla p(\boldsymbol{\xi}^-_{\mathbf{x},t}(\tau),\tau)}{\rho}\cdot d\boldsymbol{\tau}. \qquad (14)$$

For the same reasons as above, we set $C_p=0$, which results in Figure 2(f).

In analogy, the third term of Equation 13 motivates to compute the energy difference between two points along a pathline due to energy diffusion as:

$$\tilde{E}_\nu(\mathbf{x},t)=C_\nu-\int_t^{t_\alpha}\nu\Delta\mathbf{u}(\boldsymbol{\xi}^-_{\mathbf{x},t}(\tau),\tau)\cdot d\boldsymbol{\tau}, \qquad (15)$$

which we denote *integrated diffusion energy* (Figure 2(b)). Notice that $\tilde{E}_\nu$ cannot be obtained without

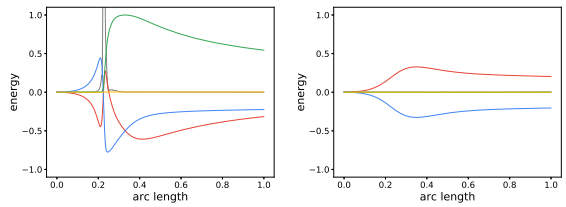

(a) (b)

Figure 3: 2D pathline plots, with $\tilde{E}_u$ (red), $\tilde{E}_p$ (blue), $\tilde{E}_\nu$ (green), $\tilde{E}_t$ (yellow), and ε (gray). (a) Plot corresponding to upper selected (gray) streamline in Figure 2. (b) Plot corresponding to lower selected (gray) streamline in Figure 2.

integration, whereas E_u and E_p could. Nevertheless, for consistency, we will work with $\tilde{E}_u$, $\tilde{E}_p$, and $\tilde{E}_\nu$.

Finally, $\tilde{E}_t(\mathbf{x},t) := \tilde{E}_u(\mathbf{x},t) + \tilde{E}_p(\mathbf{x},t) + \tilde{E}_\nu(\mathbf{x},t)$, our *integrated total energy*, is conserved along pathlines, and represents the basis for our approach. It can be seen as the counterpart to Bernoulli's principle, for unsteady viscous flow. Figure 2(h) shows $\tilde{E}_t$, and one can see that the field is constant along pathlines, in contrast to E_t (Figure 2(g)).

4.2 2D Pathline Plots

To ease visual analysis of the variation (conversion) of the energies $\tilde{E}_u$, $\tilde{E}_p$, and $\tilde{E}_\nu$ along pathlines, we introduce *2D pathline plots*. In these plots, a given pathline represents the abscissa, parametrized by arc length in flow direction. Figure 3(a) shows the plot for the upper gray pathline (which is identical to a streamline in this case) in Figure 2, whereas Figure 3(b) shows the plot for the lower gray pathline in Figure 2. In our implementation, the user can interactively seed a pathline and explore the transformation of energy along it by examining the respective plot in a linked view. It can be seen how the energies are converted and that $\tilde{E}_t$ is indeed conserved.

The upper pathline (Figure 3(a)) passes close by the obstacle. Before the obstacle, $\tilde{E}_u$ reduces and $\tilde{E}_p$ increases, indicating conversion from kinetic to pressure energy. Behind the obstacle (where the pathline resides in the low-velocity wake), $\tilde{E}_u$ is low but increasing, while $\tilde{E}_\nu$ is decaying almost at the same rate, whereas $\tilde{E}_p$ stays almost constant. This indicates that kinetic energy is transported from the outside into this region by diffusion, which means that that part of the wake is accelerated due to viscosity, but influenced by pressure only in close vicinity to the obstacle.

Energy dynamics along the lower pathline (Figure 3(b)), on the other hand, is basically not affected by viscosity. We identify from the pathline plot that the flow is first accelerated due to conversion from pressure energy to kinetic energy, and later the flow decelerates again, by transforming kinetic energy back to pressure energy.

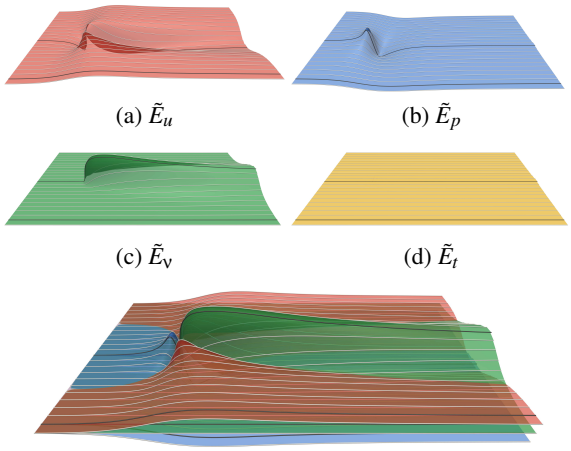

(a) $\tilde{E}_u$ (b) $\tilde{E}_p$

(c) $\tilde{E}_\nu$ (d) $\tilde{E}_t$

(e)

Figure 4: 3D pathline plots provide context for the 2D pathline plots. The front gray pathline corresponds to Figure 3(b), whereas the farther one refers to the plot form Figure 3(a). For more compact context, the surfaces can be combined into a single view (e).

4.3 3D Pathline Plots

Whereas the 2D pathline plots are an effective means for interactive analysis of energy dynamics along individual pathlines, they do not provide context, i.e., they do not give information about the relation or comparison between different pathlines. To this end, we introduce *3D pathline plots*, as a complementary technique that provides overview and context. We construct these plots by computing a rake of pathlines (i.e., a set of pathlines seeded along a straight seeding curve, e.g., as shown in Figure 2), generating the 2D plot for each of these pathlines, and then creating a mesh between "adjacent" curves of the same quantity. That is, we take for each of the quantities $\tilde{E}_u$, $\tilde{E}_p$, $\tilde{E}_\nu$ and $\tilde{E}_t$ all arc-length parametrized curves, distribute them evenly in "orthogonal" direction, and create for each of the quantities a triangle mesh. Figure 4(a)–(d) shows an example for the resulting surfaces. Notice that in Figure 2, we show only every second pathline that is used for generating the 3D plots, and for better visibility, we additionally show only the lower half.

For improved context, the selected 2D pathline is denoted by a dark gray curve both in the 2D fields, as well as on the 3D plot surfaces. For more compact overview, the resulting surfaces can also be merged (Figure 4(e)), however, in that configuration they rather serve for context than for qualitative insights, due to potential occlusion issues and clutter.

4.4 Energy Conversion Maps

Although the 3D pathline plots provide good context for interactive exploration by means of 2D pathline plots, they exhibit several shortcomings for qualitative or even quantitative analysis.

First, as mentioned above, their merged representation (Figure 4(e)) tends to suffer from occlusion and visual clutter. Second, the fact that they do not represent the spatial domain but instead a space that is spanned by pathline arc length and pathline index hinders interpretation. Third, we set the constants C_u, C_p, and C_ν to zero, but any choice would be possible, which makes the "offset height" of the individual pathline curves in the 3D pathline plot surfaces basically meaningless, including their intersection (e.g., the intersection between the red and green manifold in Figure 4(e)). Since the final goal of our work is the analysis of conversion of different types of energy, it is rather the rate of change of these energies along a pathline that is of interest, than their value itself. This motivates us to use material derivatives of $\tilde{E}_u$, $\tilde{E}_p$, and $\tilde{E}_\nu$ for a more qualitative and quantitative analysis.

The material derivative is a differentiation with respect to time-dependent flow, and it captures the rate of change of a quantity, as "observed" along a pathline. Thus, the material derivative of $\tilde{E}_u$, $\tilde{E}_p$, and $\tilde{E}_\nu$ gives us the amount of energy type per time unit that is gained or lost by means of energy conversion along a pathline. We could plot these derivatives again by means of the 3D pathline plot approach (see Figure 5(a) for an example). Whereas this would solve the issue with the constants, since they vanish in the derivative, this representation would still suffer from occlusion, visual clutter, and non-spatial domain. Therefore, we present *energy conversion maps*, our final component that complements our already presented building blocks.

Our energy conversion maps are 2D RGB images in case of 2D flow. For $\tilde{E}_u$, we compute its material derivative $D\tilde{E}_u(\mathbf{x},t)/Dt$, determine the 5th percentile P_5 and the 95th percentile P_{95} of the material derivative, obtain the maximum P_m of $|P_5|$ and $|P_{95}|$, and then linearly map the material derivative to the red channel, mapping $-P_m$ to zero red value and P_m to full red value. Analogously, we map the material derivative of $\tilde{E}_\nu$ to the green channel, and the material derivative of $\tilde{E}_p$ to the blue channel. This means, that if all material derivatives are zero, this will result in medium gray color. Figure 5(b) shows a respective result, corresponding to Figure 5(a).

The light blue region in front of the obstacle in Figure 5(b), for example, corresponds to conversion of kinetic to pressure energy. The orange region to the sides of the obstacle, on the other hand, indicates conversion of pressure energy to kinetic energy. The purple region behind the obstacle, i.e., in its wake, represents conversion from diffusion energy to both kinetic and pressure energy. Finally, the greenish parts on either side of the purple wake indicate conversion from kinetic and pressure energy to diffusion energy, which means that the greenish regions "give" their energy to the purple one via viscous interaction.

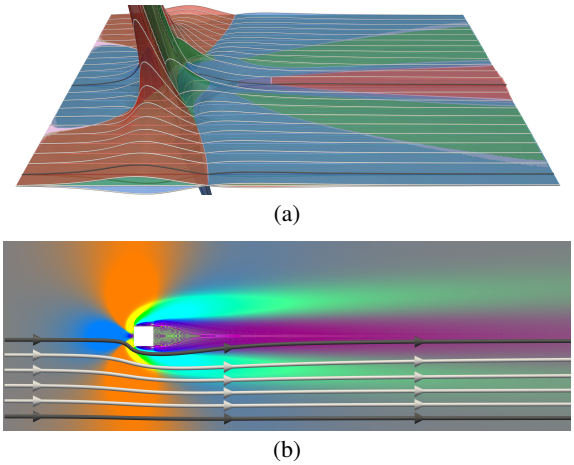

(a)

(b)

Figure 5: (a) 3D plot representation of material derivatives of $\tilde{E}_u$ (red), $\tilde{E}_p$ (blue), and $\tilde{E}_\nu$ (green). (b) Energy conversion map, mapping to red, green, and blue color channel.

5 RESULTS

Having in place our overall technique, we will apply it now to different datasets. First, we examine a slightly time-dependent flow around an obstacle (Section 5.1), followed by a more unsteady case exhibiting a Kármán vortex street (Section 5.2). Finally, we demonstrate that our approach is also applicable to advanced flow problems, such as the flow through elastic porous media (Section 5.3).

5.1 Slightly Unsteady Obstacle Flow

We now examine a CFD simulation that has been simulated on the same geometry as the above steady obstacle flow, but with higher inlet velocity. As a consequence, the flow is slightly time-dependent, i.e., the wake behind the obstacle is "oscillating". Figure 6(a) shows streamlines of a snapshot of the time-dependent flow, whereas Figure 6(b)–(e) show the pathlines used for plot-based visualization. Notice that $\tilde{E}_u$, $\tilde{E}_p$, $\tilde{E}_\nu$, and $\tilde{E}_t$ are not consistent with the pathlines, since these fields are computed by a large set of reverse-integrated pathlines started at each point

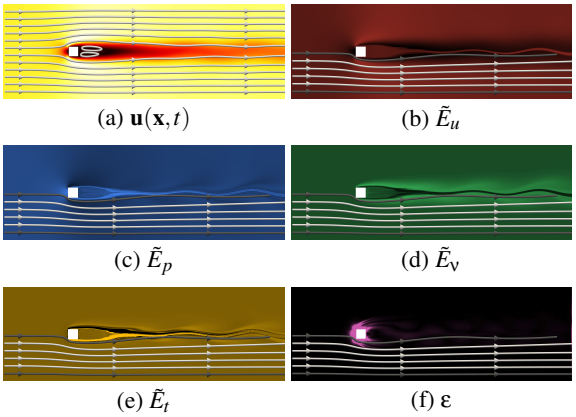

Figure 6: Slightly unsteady obstacle flow. (a) Velocity magnitude with streamlines. (b) Integrated kinetic energy with pathlines (white and gray). (c) Integrated pressure energy. (d) Integrated diffusion energy. (e) Integrated total energy. (f) Solver error.

in space, as explained above, and therefore are located at different space-time location. Nevertheless, a look at the respective pathline plots (Figure 7(a) for the upper gray pathline and Figure 7(b) for the lower one) reveals that $\tilde{E}_t$ is still conserved very well along these pathlines. A closer inspection of Figure 7(a) reveals that $\tilde{E}_t$ slightly increases when the pathline passes the obstacle. This is consistent with higher values of the solver error ε there. Overall, investigating the 3D pathline plots (Figure 7(c)–(g)) and the energy conversion map (Figure 7(h)) reveals that this flow is still similar to the steady one from Section 4, and that our approach works equally well with pathlines in time-dependent flow.

5.2 Kármán Vortex Street

This example is the result of increasing the inlet velocity even more, resulting in Kármán vortex shedding. As can be seen from the different energy fields and the comparison between streamlines (Figure 8(a)) and pathlines (Figure 8(b)–(e)), this dataset is substantially time-dependent. Furthermore, it exhibits larger solver error ε (Figure 8(f)) than the one from Section 5.1. This larger error leads to a lower level of energy conservation at the obstacle, as can be seen from the variation of $\tilde{E}_t$ in the 2D pathline plot for the upper pathline (Figure 9(a)). In contrast, energy is well conserved for the lower pathline (Figure 9(b)), consistent with the lower solver error in that region.

The energy conversion map (Figure 9(h)) reveals that the area around the vortex shedding is dominated by conversion from kinetic to pressure energy (light blue), and back from pressure energy to kinetic energy (orange). Close to the Lagrangian coherent

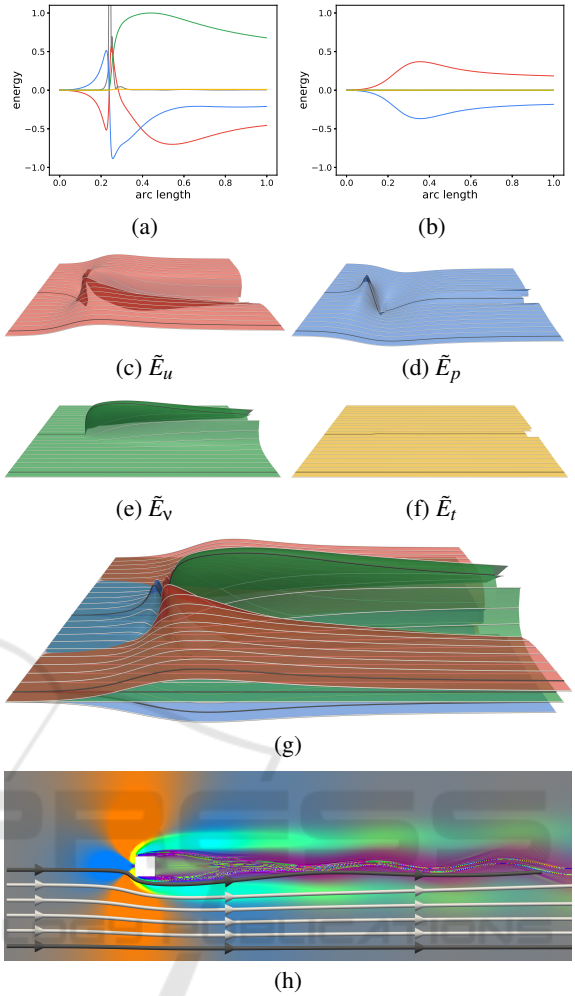

Figure 7: Slightly unsteady obstacle flow. 2D pathline plot for upper (a) gray pathline from Figure 6(b) and lower (b) one. 3D pathline plots (c)–(g). (h) Energy conversion map reveals similarity with steady example from Section 4.

structures (ridges in the reverse finite-time Lyapunov exponent field (Figure 9(i)), computed for the same integration time as our energies), our approach indicates conversion from kinetic and pressure energy to diffusion energy (green), and back from diffusion energy to kinetic and pressure energy (purple). This may indicate, similar to the case from Figure 5(b), that energy is transported via viscous mechanisms (diffusion). Besides that, the dark blue regions indicate conversion from kinetic and diffusion energy to pressure energy, and the yellow regions back from pressure to kinetic and diffusion energy, also relating to viscous effects. Nevertheless, a more detailed analysis and validation regarding the impact of ε has to be subject to future work.

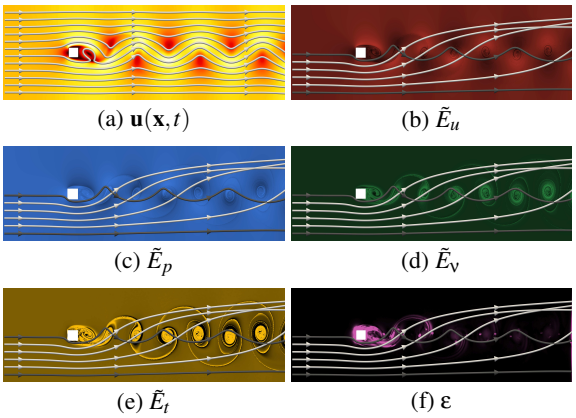

(a) $\mathbf{u}(\mathbf{x},t)$ (b) $\tilde{E}_u$ (c) $\tilde{E}_p$ (d) $\tilde{E}_\nu$ (e) $\tilde{E}_t$ (f) ε

Figure 8: Kármán dataset. (a) Velocity magnitude with streamlines (white). Kinetic (b), pressure (c), diffusion (d), and total energy (e). Solver error (f) is considerably higher compared to the slightly unsteady case (Figure 6(f)).

5.3 Elastic Porous Flow

Our last example is a simulation of a flow through an elastic porous medium. In this case, it is the solution of the consolidation model of Biot, which averages the porous medium to macroscopic scale. The setup, which is quadratic in rest state, exhibits three different permeabilities (Figure 11(a)). The upper and lower boundaries are non-permeable, the left boundary is a velocity inlet, and the right boundary serves as a "valve", i.e., the permeability is very low during the first phase, and high during the second phase. As a consequence, the material is first "inflated", and starts releasing the fluid after the inflow has been stopped and the right boundary has been "opened".

Since this example consists of an elastic porous medium, within which energy can be stored as pressure and deformation, we replace the material derivative of energies by the time derivative, i.e., we focus on the material instead of the flow through the material. Also, due to the used simulation model, we do not need to take into account diffusion caused by viscosity. Thus, diffusion energy from above is replaced by deformation energy, which we compute as

$$E_d := \frac{1}{2}\int_C \|\nabla \mathbf{d}(\mathbf{x},t) + (\nabla \mathbf{d}(\mathbf{x},t))^\top\|^2 d\mathbf{x} + \int_C |\nabla \cdot \mathbf{d}(\mathbf{x},t)|^2 d\mathbf{x}, \tag{16}$$

with displacement field $\mathbf{d}(\mathbf{x},t)$ and cell C of the grid.

Figure 10(a)–(c) shows the first phase of the process for kinetic energy, (f)–(h) for pressure energy, and (k)–(m) deformation energy. Accordingly, (c)–(e) shows the second phase for kinetic energy, (h)–(j) for pressure energy, and (m)–(o) for deformation energy. Figure 11(b) depicts energy dynamics at the center.

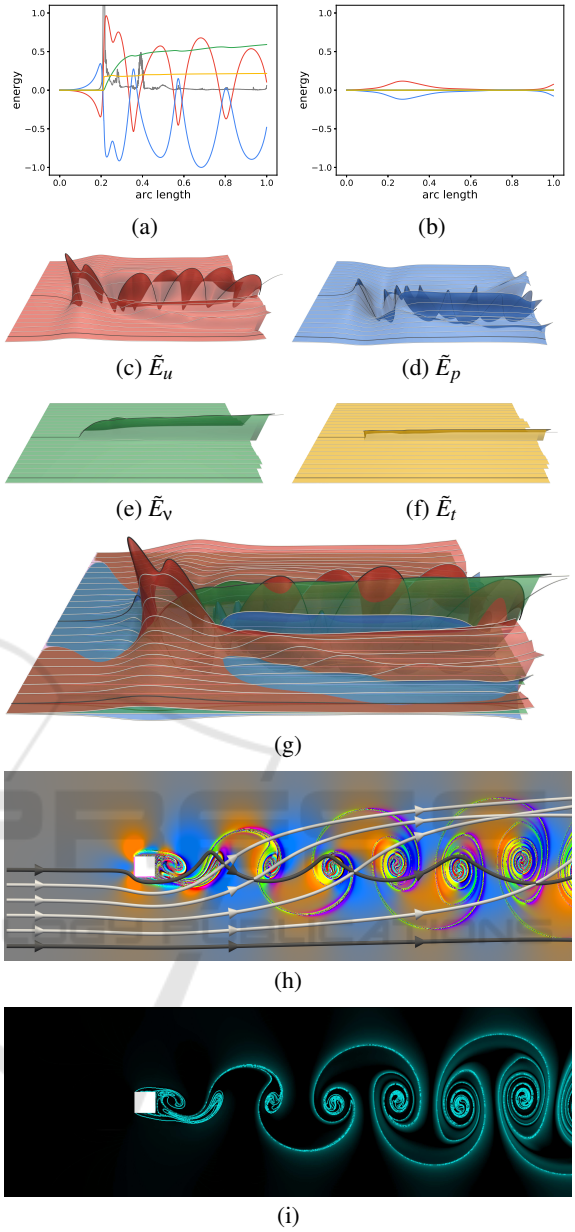

(a) (b) (c) $\tilde{E}_u$ (d) $\tilde{E}_p$ (e) $\tilde{E}_\nu$ (f) $\tilde{E}_t$ (g) (h) (i)

Figure 9: Kármán flow. 2D pathline plots (a) and (b) reveal that energy conservation is violated close to the obstacle due to high solver error (Figure 8(f)) in that region. 3D pathline plots (c)–(g) reflect energy dynamics of vortex shedding. (h) Energy conversion map. (i) Finite-time Lyapunov exponent field, for comparison (low-black; high-cyan).

The three phases and respective energy conversions are clearly visible in the plot. It is apparent that during the inflation phase, kinetic energy is higher at the inlet, whereas during the outflow phase, kinetic energy is larger at the outlet. Interestingly, pressure energy as well as deformation energy are larger at the inlet in both phases. The energy conversion maps (Figure 10(p)–(t)), based on the time derivative, reveal

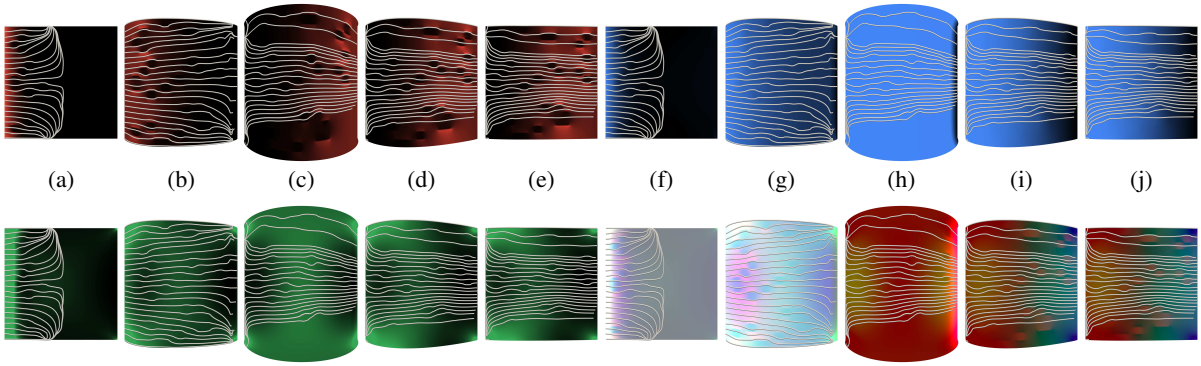

Figure 10: Elastic porous flow. (a)–(e) Kinetic energy, (f)–(j) pressure energy, (k)–(o) deformation energy, and (p)–(t) respective energy conversion maps, each with respective streamlines.

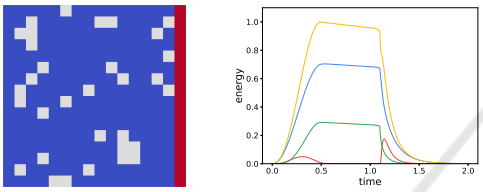

(a) (b)

Figure 11: Elastic porous flow. (a) High (blue), medium (gray), and very low (red) permeability. (b) Plot of kinetic (red), pressure (blue), deformation (green), and total (yellow) energy over time, at the center of the domain.

that during the first phase, energy conversion is low (close to gray colors), whereas at the start of the second phase, one can see conversion from pressure and deformation energy to kinetic energy, in particular at the outlet. During the second phase, we observe that the region that converts deformation and pressure into kinetic energy shrinks from right to left.

6 CONCLUSION

We presented a counterpart to Bernoulli's principle, which describes the conservation and conversion of energy along streamlines in inviscid flow. By extending the concept to time-dependent flow and accounting for viscous effects, we established a basis for the visualization of energy dynamics in flow fields. We presented an interactive exploration approach based on our concept, complemented it with a direct visualization approach of energy conversion, and demonstrated its utility using simple examples. As future work, we would like to further investigate the properties of our approach using additional examples, and extend it to 3D flow fields and other types of energy.

ACKNOWLEDGEMENTS

The research leading to these results has been done within the Transregional Collaborative Research Center SFB / TRR 165 "Waves to Weather" funded by the German Science Foundation (DFG).

REFERENCES

Barth, W. and Burns, C. (2007). Virtual rheoscopic fluids for flow visualization. *IEEE Transactions on Visualization and Computer Graphics*, 13(6):1751–1758.

Bernoulli, D. (1738). *Hydrodynamica, sive de viribus et motibus fluidorum commentarii. Opus academicum ab auctore, dum Petropoli ageret, congestum.*

Brownlee, C., Pegoraro, V., Shankar, S., McCormick, P., and Hansen, C. (2010). Physically-based interactive schlieren flow visualization. In *Proc. IEEE Pacific Visualization Symposium 2010*, pages 145–152.

Fernandes, O., Frey, S., and Ertl, T. (2017). Transportation-based visualization of energy conversion. In *Proc. IVAPP 2017*, volume 3, pages 52–63.

Jeong, J. and Hussain, F. (1995). On the identification of a vortex. *Journal of Fluid Mechanics*, 285(69):69–94.

Pobitzer, A., Tutkun, M., Andreassen, O., Fuchs, R., Peikert, R., and Hauser, H. (2011). Energy-scale aware feature extraction for flow visualization. *Computer Graphics Forum*, 30(3):771–780.

Popinet, S. (2007). The Gerris flow solver. In *Rencontres Mondiales du Logiciel Libre, July*.

Sadlo, F., Peikert, R., and Sick, M. (2006). Visualization tools for vorticity transport analysis in incompressible flow. *IEEE Transactions on Visualization and Computer Graphics*, 12(5):949–956.

Schafhitzel, T., Baysal, K., Vaaraniemi, M., Rist, U., and Weiskopf, D. (2011). Visualizing the evolution and interaction of vortices and shear layers in time-dependent 3D flow. *IEEE Transactions on Visualization and Computer Graphics*, 17(4):412–425.